Lawrence Berkeley National Laboratory

Title

Correlation studies of fission-fragment neutron multiplicities

Permalink

Journal

ISSN

Authors

Albertsson, M
Carlsson, BG
Døssing, T
et al.

Publication Date

DOI

Correlation studies of fission fragment neutron multiplicities

M. Albertsson,[1] B.G. Carlsson,[1] T. Døssing,[2] P. Möller,[1,3] J. Randrup,[4] and S. Åberg[1]

[1]*Mathematical Physics, Lund University, S-221 00 Lund, Sweden*
[2]*Niels Bohr Institute, University of Copenhagen, 2100 Copenhagen Ø, Denmark*
[3]*P. Moller Scientific Computing and Graphics, Inc., P.O. Box 75009, Honolulu, HI 96836 USA*
[4]*Nuclear Science Division, Lawrence Berkeley National Laboratory, Berkeley, California 94720, USA*
(Dated: May 21, 2020)

We calculate neutron multiplicities from fission fragments with specified mass numbers for events having a specified total fragment kinetic energy. The shape evolution from the initial compound nucleus to the scission configurations is obtained with the Metropolis walk method on the five-dimensional potential-energy landscape, calculated with the macroscopic-microscopic method for the three-quadratic-surface shape family. Shape-dependent microscopic level densities are used to guide the random walk, to partition the intrinsic excitation energy between the two proto-fragments at scission, and to determine the spectrum of the neutrons evaporated from the fragments. The contributions to the total excitation energy of the resulting fragments from statistical excitation and shape distortion at scission is studied. Good agreement is obtained with available experimental data on neutron multiplicities in correlation with fission fragments from ^{235}U(n$_{th}$,f). At higher neutron energies a superlong fission mode appears which affects the dependence of the observables on the total fragment kinetic energy.

Keywords: Fission, Brownian shape evolution method, Microscopic level densities, Correlations

I. INTRODUCTION

A long-standing challenge in nuclear fission is the dependence of the average neutron multiplicity $\bar{\nu}$ on the fragment mass number A. The characteristic sawtooth behavior of $\bar{\nu}(A)$ is well illustrated for ^{235}U(n$_{th}$,f), see e.g. Ref. [1]. Because the number of neutrons evaporated is indicative of the excitation energy in the emitting fragment, it is of key importance to understand the degree of excitation of the fission fragments, as a function of A.

To a good approximation, the total excitation energy of a given fission fragment is the sum of two distinct contributions. One is the share of total statistical excitation received by the distorted proto-fragment at the time of scission. The other contribution results from the relaxation of the fragment shape from its distorted form at scission to its equilibrium shape which converts the change in potential energy into additional fragment heat. Different theoretical descriptions of the fission process [2–7] have yielded different results for the amount of distortion energy. Furthermore, because it is the sum of the two contributions that determines the energy available for neutron evaporation, it is difficult to determine the individual contributions from the measured $\bar{\nu}(A)$ alone.

However, by studying the dependence of $\bar{\nu}(A)$ on the total fragment kinetic energy (TKE) it may be possible to gain important insight into how the fission fragment excitation energy is composed. Such correlation measurements were performed recently, yielding $\bar{\nu}(A; \mathrm{TKE})$ for ^{235}U(n$_{th}$,f) [8]. In this paper, we discuss how variations of TKE are associated with structure-dependent variations in the contributions to the fission fragment excitations, leading in turn to observable variations of the TKE-constrained neutron multiplicity, $\bar{\nu}(A; \mathrm{TKE})$.

Due to the highly dissipative character of collective nuclear dynamics, it has proven possible to model the shape evolution of a fissioning nucleus as a Metropolis walk on the multi-dimensional potential-energy surface [9–11]. By using shape-dependent microscopic level densities [12] for guiding the shape evolution, a consistent framework was obtained for calculating the energy-dependent fission-fragment mass distribution [13].

However, in the region of symmetric fission the scission configurations lead to too little statistical excitation [7] and to too high TKE. While this problem is of little importance as long as the focus is on the fragment-mass yields (which tend to be very small in the symmetric region), it is relevant for the calculation of $\bar{\nu}(A)$. Therefore, in the present study of correlated neutron multiplicities, we consider only fission events in the asymmetric region, namely $A_L \leq 104$ (and correspondingly $A_H \geq 132$).

Recently, shape-dependent microscopic level densities were employed also for the calculation of the excitation energy partition between the fission fragments [7]. In that treatment, it was assumed that the statistical excitation energy available at scission is divided microcanonically between the two proto-fragments whose distorted shapes later on relax to their ground-state forms. It was found [7] that this treatment leads to a reasonably good reproduction of $\bar{\nu}(A)$ measured for ^{235}U(n,f) at both thermal energies and $E_n = 5.55$ MeV [14], in particular for asymmetric fission events. The study brought out the important influence of the specific structure of the various proto-fragments whose level densities affect the energy partitioning significantly.

We now go further and study the energy dependence of the structure effects by gating on specific values of TKE. In such a more detailed study, the specification of a particular TKE value selects the total excitation energy TXE. The resulting fragment excitation energies can then be calculated and the associated mean neutron mul-

tiplicities, $\bar{\nu}(A; \text{TKE})$, can be obtained.

Thus, for the first time, a fission model based on microscopic level densities, combined with a 5D potential-energy surface obtained with the macroscopic-microscopic method, is applied to calculate more complex correlation observables, namely the average neutron multiplicity from fission fragments of given A for events with a particular TKE. A phenomenological deterministic model of prompt neutron emission was recently applied to the same problem yielding very good agreement with data [17].

The method of the calculation is briefly presented in Sect. II. In Sect. III we discuss contributions from intrinsic and distortion energy at scission to the excitation energies of the primary fission fragments, and in Sect. IV the results for the neutron multiplicities are presented. Finally, Sect. V presents a summary and a discussion.

II.   METHOD OF CALCULATION

The calculations closely follow Ref. [7]. The evolution of the nuclear shape from the ground-state shape to scisson is treated as a Metropolis random walk on the potential-energy landscape $U(\boldsymbol{\chi})$ [9]. The shape $\boldsymbol{\chi}$ is described by the 3QS parametrization [15, 16] which has five parameters: the overall elongation given by the quadrupole moment q_2, the neck radius c, the spheroidal deformations ε_{f1} and ε_{f2} of the endcaps of the two nascent fragments, and the mass asymmetry α. For each of the more than 6 million nuclear shapes considered, the microscopic level density is calculated by the combinatorial method [12] up to about 6 MeV of excitation energy and is extrapolated to higher energies using the calculated shell and pairing energies [13].

The initial configuration is assumed to be a compound nucleus having the excitation energy $E_0^* = E_{\text{n}} + S_{\text{n}}$, where E_{n} is the kinetic energy of the incoming neutron being absorbed and S_{n} is the corresponding neutron separation energy. With M_0 as the mass of the compound nucleus, the total energy is given by $E_{\text{tot}} = M_0 + E_0^*$ which is conserved during the subsequent evolution. Consequently, at a given shape $\boldsymbol{\chi}$ the local intrinsic energy is given by $E^*(\boldsymbol{\chi}) = E_{\text{tot}} - U(\boldsymbol{\chi})$ because the shape motion is assumed to be so strongly damped that the local collective kinetic energy is negligible.

In the considered fission reaction $^{235}\text{U}(\text{n,f})$ the compound nucleus ^{236}U can have either angular momentum $I = 3$ or 4. The angular momentum is conserved in the Metropolis random walk by considering level densities with a fixed angular momentum for each shape. Since $I = 3$ and 4 give very similar result [13] the presented calculations are performed at $I = 4$.

As in our earlier work [13], the shape changes are selected by the Metropolis method using the associated shape-dependent microscopic level densities $\rho(\boldsymbol{\chi})$, ensuring detailed balance, $P(\boldsymbol{\chi} \rightarrow \boldsymbol{\chi}')/P(\boldsymbol{\chi}' \rightarrow \boldsymbol{\chi}) = \rho(\boldsymbol{\chi}')/\rho(\boldsymbol{\chi})$.

The asymmetry α is asssumed to be frozen in when the neck radius has shrunk to $c = c_0 = 2.5$ fm [7, 13]. Subsequently, the system reaches a scission configuration at $c = c_{\text{sc}} = 1.5$ fm [7] where the shapes of the proto-fragments are determined (see Sect. III B), and the available intrinsic energy is partitioned between them (see Sect. III A). The initially distorted proto-fragments are being accelerated by their mutual Coulomb repulsion and the shapes eventually revert to equilibrium forms. Their original distortion energies are thereby converted to additional intrinsic excitation. Subsequently, after full acceleration has been achieved, each excited primary fragment evaporates neutrons as long as it is energetically possible (see Sect. IV).

For each reaction case considered, a total of 10^6 fission events are generated and for each one we record the mass numbers of the two primary fission fragments, A_{L} and A_{H}, their total kinetic energy TKE, as well as the number of neutrons evaporated from each one, ν_{L} and ν_{H}, as would be done in an ideal experiment.

III.   ENERGIES IN THE FISSION PROCESS

In Sect. III A we discuss the various key energies, namely the total fragment excitation energy (TXE) and the corresponding total fragment kinetic energy (TKE), as well as the decomposition of the individual proto-fragment excitations into intrinsic and distortion energies. Then, in Sect. III B we describe how the intrinsic energy available at scission is partitioned between the two proto-fragments and how this depends on TKE. Finally, in Sect. III C we analyze the variation of the distortion energy with TKE and fragment mass.

A.   Key energy quantities

Once the initial compound nucleus has been prepared, we follow an ensemble of shape evolutions, as described in Sect. II. These represent possible evolutions of the fissioning system subject to the conservation of the total energy E_{tot}. When the evolving system has attained its scission shape, $\boldsymbol{\chi}_{\text{sc}}$, it is assumed to divide into two distorted and excited proto-fragments which subsequently recede and accelerate while their shapes gradually relax to their equilibrium forms.

We assume that the strongly damped description of the shape evolution remains valid until scission, so the proto-fragments are formed with vanishing kinetic energy. Furthermore, the fragments typically carry several (≈ 4) units of angular momentum, but we ignore the associated rotational energy which is relatively small. The combined intrinsic excitation energy of the two proto-fragments at scission is then given by the corresponding local intrinsic energy,

$$E_{\text{L}}^{\text{intr}} + E_{\text{H}}^{\text{intr}} = E^*(\boldsymbol{\chi}_{\text{sc}}) = E_{\text{tot}} - U(\boldsymbol{\chi}_{\text{sc}}) . \qquad (1)$$

The partitioning of the intrinsic energy among the two fragments is assumed to be statistical (see Sect. III B).

For a given mass partition, $A_0 \to A_L + A_H$, the Q value is $Q_{LH}^* = M_0 + E_0^* - M_L - M_H$. This quantity represents the energy available for the total fragment kinetic energy, TKE, and the combined excitation energies of the two primary fragments, TXE, after the acceleration and the shape relaxation have been completed,

$$Q_{LH}^* = \text{TKE} + E_L^* + E_H^* = \text{TKE} + \text{TXE} . \qquad (2)$$

In the present study, we assume that the proto-fragments have spheroidal shapes with eccentricities equal to those of the corresponding endcaps of the 3QS scission shape, $\varepsilon_{L,sc} = \varepsilon_{f1}(\boldsymbol{\chi}_{sc})$ and $\varepsilon_{H,sc} = \varepsilon_{f2}(\boldsymbol{\chi}_{sc})$. The distortion energy of proto-fragment $i = L, H$ can then be expressed as $E_i^{dist} = U_i(\varepsilon_{i,sc}) - U_i(\varepsilon_{i,gs})$, where $U_i(\varepsilon)$ denotes the potential energy of deformation of the fragment (see Sect. III C). As the proto-fragments gradually attain their ground-state shapes, their distortion energies are being converted into additional intrinsic excitation energy, so the final excitation energy is the sum of the original intrinsic energy at scission and the distortion energy,

$$E_L^* = E_L^{intr} + E_L^{dist} , \quad E_H^* = E_H^{intr} + E_H^{dist} . \qquad (3)$$

Thus, with $\text{TXE} = E_L^* + E_H^*$, the total kinetic energy is determined from Eq. (2), $\text{TKE} = Q_{LH}^* - \text{TXE}$.

Figure 1 shows contour plots of the calculated (a) and measured (b) number of scission events with respect to fragment mass number A and total fragment kinetic energy TKE for $^{235}\text{U}(n_{th}, f)$.

In the region of symmetric fission, the measured TKE values are considerably lower than the calculated values. This is probably caused by too small elongations of the calculated fission configurations at scission that leads to too small statistical excitation and an overestimation of the TKE. Due to this problem, we restrict the present study to asymmetric fission.

In the asymmetric region ($A_L \leq 104$ and $A_H \geq 132$), the measured most probable TKE shows a gradual decrease with increasing asymmetry. This feature is well reproduced by the calculations.

However, the width of the TKE distribution for a given A is underestimated in the calculation by typically 20%. This may (at least in part) be due to the fact that the calculations include only even-even fragment pairs having (approximately) equal N/Z ratios, namely that of ^{236}U. As a consequence of this restriction, there is only one (N, Z) combination for a given A, whereas the actual fission process populates several combinations and thus leads to a broader TKE distribution.

The fixed (N, Z) combination for given fragment mass number A, assumed in the calculations, implies a well defined Q value, shown by a dashed curve in Fig. 1a. This constitutes the maximum possible value of TKE $\text{TKE}_{max}(A) = Q^*(A)$, and the bulk of the events lie well below this boundary. In experiments different (N, Z)

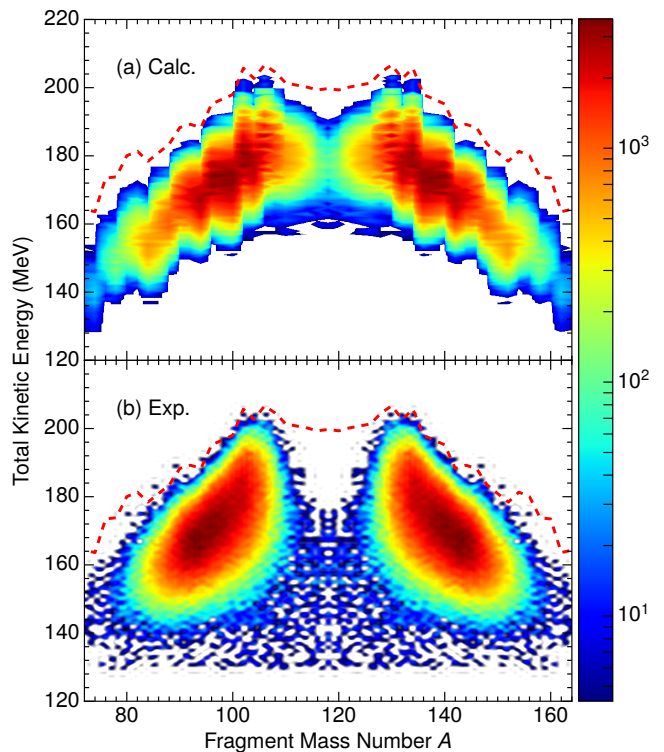FIG. 1. Number of scission events in log-scale versus fission fragment mass number and total kinetic energy for $^{235}\text{U}(n_{th}, f)$. In (a) calculated results with c_0=1.5 fm, and in (b) experimental data from Ref. [18]. The dashed curve shows Q values for different fragment masses. Experimental number of events are scaled to the same number of events as calculated, namely 10^6.

combinations are possible for each A, leading to a set of Q values. However, in Fig. 1b we show the Q values from Fig. 1a.

For a given mass asymmetry (and thus a given Q value), the variation of TKE is counterbalanced by the variation of TXE, the combined excitation of the primary fragments. Consequently, by gating on TKE it is possible to investigate a TXE range of about 10-40 MeV, for a given asymmetry. In particular, if, for a given mass partition, the specified TKE value is gradually decreased, starting from the maximally realized value, the available TXE will exhibit a corresponding gradual increase. This, in turn, will be reflected in the mean number of neutrons evaporated from each of the two fragments, $\bar{\nu}_L$ and $\bar{\nu}_H$, which will provide more detailed experimental information on the origin of E_L^* and E_H^*.

In general, a fission event having a small TKE value (i.e. a large TXE value) is associated with a rather elongated scission configuration, as measured for example by the quadrupole moment of the density distribution, q_2. This feature is illustrated quantitatively in Fig. 2 showing contour plots of the number of scission events versus TKE and q_2 for the mass split, $A_L : A_H = 104 : 132$ for E_n=0 (a) and E_n=5.55 MeV (b). At E_n=0 a wide
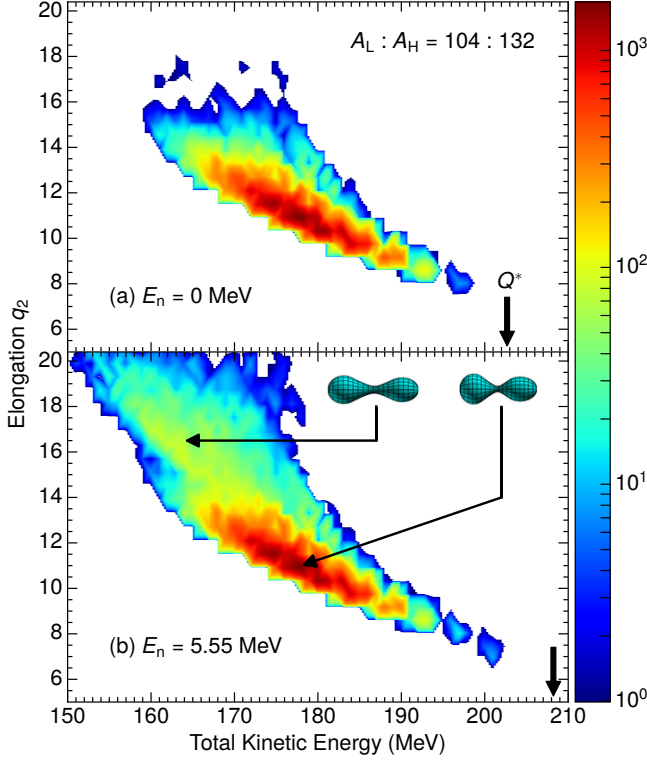
FIG. 2. Number of scission events in log-scale for fragment mass division A_L:A_H=104:132 versus total kinetic energy TKE and elongation q_2. In (a) E_n=0 and in (b) E_n=5.55 MeV. In (b) typical shapes are shown for the superlong ($q_2 \approx 16.5$) and standard ($q_2 \approx 11$) modes. Arrows indicate the Q^*-values.

range of quadrupole moments occur, $8 < q_2 < 18$, for the considered mass partition. The most compact scission shapes (having the smallest q_2 values) are associated with large TKE values close to the Q value, while the most elongated scission shapes (having the largest q_2 values) have TKE values that are about 40 MeV smaller. The scission shapes are thus strongly dependent on the considered TKE value.

In Fig. 2b we show that even more elongated scission shapes can occur when more energy is made available by increasing the kinetic energy of the incident neutron. This is related to the appearance of a superlong fission mode. In 4-D Langevin calculations [19] the symmetric fission events at low TKE (140-170 MeV) seen in Fig. 1b, valid for thermal neutrons, could be related to the superlong mode. With increasing excitation energy this fission mode becomes important also for asymmetric fission, that is discussed in Sect. IV C.

B. Intrinsic excitation energies

We assume that the intrinsic excitation energy available at scission, E_{sc}^*, is divided statistically between the
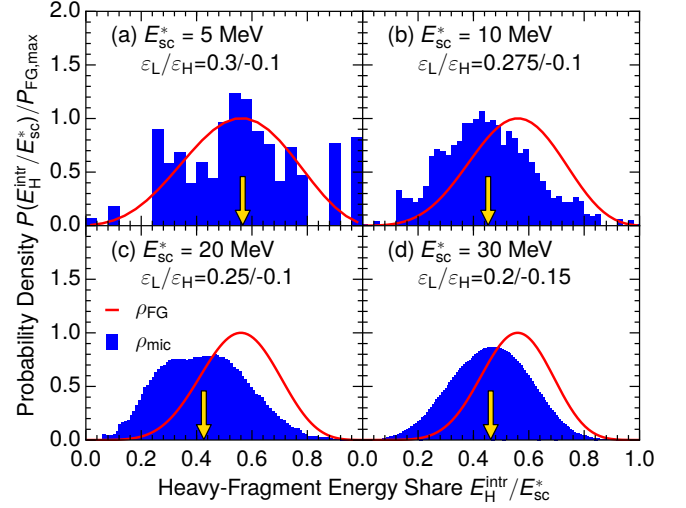

FIG. 3. Probability density for the heavy-fragment share E_H^{intr}/E_{sc}^* for different intrinsic energies $E_{sc}^* = E_L^{intr} + E_H^{intr}$ for the fragment mass division A_L:A_H=104:132. The blue histogram is obtained utilizing microscopic level densities and the red curve utilizing Fermi-gas level densities. In (a) E_{sc}^* =5 MeV, (b) E_{sc}^* =10 MeV, (c) E_{sc}^* =20 MeV, and (d) E_{sc}^* =30 MeV. Deformations of heavy and light fragments, $\varepsilon_L/\varepsilon_H$, are average values at given total excitation energy. Arrows mark the average energy from microscopic level densities.

two proto-fragments, as proposed in Ref. [7]. Thus the probability distribution for the intrinsic excitation of the heavy fragment, E_H^{intr}, has a microcanonical form,

$$P(E_H^{intr}; E_{sc}^*) \sim \rho_H(E_H^{intr}; \varepsilon_{H,sc}) \, \rho_L(E_{sc}^* - E_H^{intr}; \varepsilon_{L,sc}),$$
(4)

where $\rho_H(E^*)$ and $\rho_L(E^*)$ are the effective level densities of the heavy and light proto-fragments evaluated at their respective shapes at scission. Figures 3 and 4 show the energy distribution function $P(E_H^{intr}; E_{sc}^*)$ for typical scission shapes for fission of ^{236}U into ^{104}Zr + ^{132}Te and ^{88}Se + ^{148}Ce, respectively, in each case for four different values of the total available energy, $E_{sc}^* = 5, 10, 20, 30$ MeV.

The distribution functions in Eq. 4, based on microscopic level densities, are compared to the corresponding distribution functions based on simple Fermi-gas level densities in Figs. 3 and 4. Both types of level density yield rather broad distributions due to the smallness of the nuclear system. However, while the Fermi-gas form gives smooth distributions that peak where the energy share equals the mass share, $E_H^{intr}/E_{sc}^* = A_H/A_0$, the microscopic level densities lead to distributions that exhibit significant irregularities at low total excitation energies. Furthermore, importantly, at low values of E_{sc}^* the most probable fragment excitation may differ significantly from the macroscopic expectation given by the Fermi-gas form. Generally, as the total excitation energy is increased, these nuclear-structure effects diminish and the microscopic energy distribution grows ever smoother
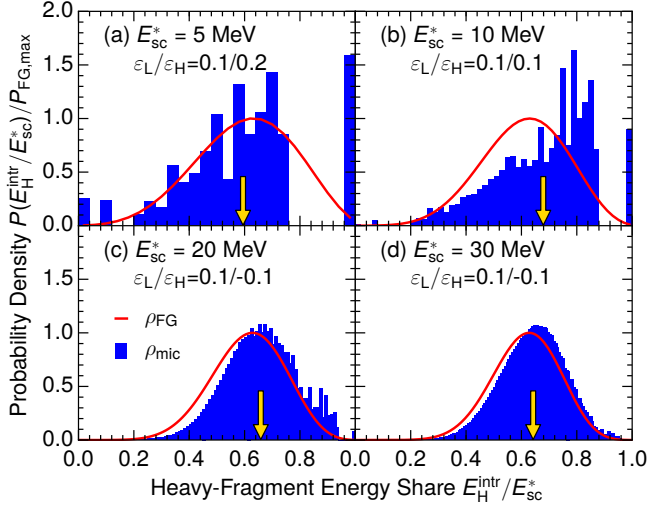
FIG. 4. Similar to Fig. 3 but for $A_L:A_H$=88:148.

FIG. 5. The average of intrinsic energy and distortion energy as functions of the total kinetic energy for six fragment combinations: (a) $A_L:A_H$=76:160, (b) 82:154, (c) 88:148, (d) 94:142, (e) 100:136, and (f) 104:132, valid for $E_n = 0$. The intrinsic energy for the heavy and light fragments is shown by solid red and blue lines, respectively. Distortion energies are shown by dashed red and blue lines, respectively. The arrows point to the Q^* values.

as it gradually approaches the Fermi-gas result.

In the example shown in Fig. 3, the heavy fragment, ^{132}Te, is close to being doubly magic and has a large negative shell energy. It therefore requires a relatively high excitation energy to approach the Fermi-gas result. Furthermore, the low level density of this fragment causes the light fragment, ^{104}Zr, to be favored in the energy sharing at most excitation energies. For example, when the available total excitation energy is E_{sc}^*=10 MeV (Fig. 3b), on the average about 6 MeV goes to the light fragment ^{104}Zr and only about 4 MeV goes to the heavy fragment ^{132}Te, while the Fermi-gas level densities lead to the reverse energy partitioning.

The other example (Fig. 4) is a somewhat more asymmetric mass division, ^{88}Se + ^{148}Ce, and some favoring of the heavy fragment is apparent, in particular at low values of E_{sc}^*. A quite spectacular situation emerges at the lowest energy shown, $E_{sc}^* = 5$ MeV, where it is predicted that the heavy fragment acquires all the energy with a non-negligible probability ($\approx$14%). This is partly due to large pairing gaps (thus low level density) for the light fragment ^{88}Se, causing the heavy fragment ^{148}Ce to be favored in the energy partitioning.

The excitation energy partition between the heavy and the light fragments may thus change significantly with the amount of total excitation energy available and, furthermore, the partition scenario may change dramatically from one pair of fission fragments to another.

With this background, we now consider the average values of the intrinsic excitation energies as well as the distortion energies of the proto-fragments resulting from the ensemble of scission configurations obtained with the Metropolis shape evolution. Figure 5 shows the average intrinsic energy of the heavy and light fragment versus the specified value of TKE, for six selected fragment-pair combinations. These examples are chosen to cover the full fragment-mass region considered:
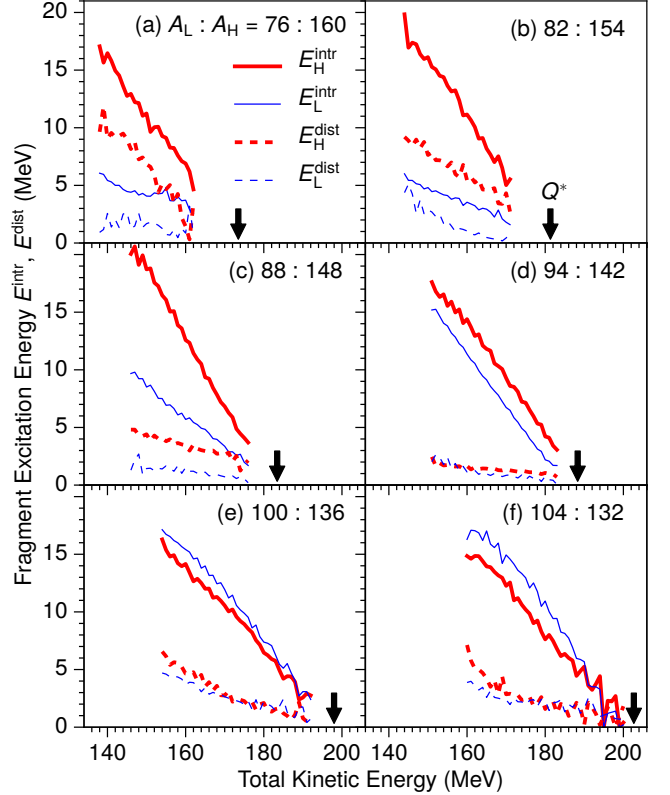
$A_L:A_H =$ 76:160 (a), 82:154 (b), 88:148 (c), 94:142 (d), 100:136 (e), and 104:132 (f).

Large nuclear-structure effects are apparent. In particular, the large share of intrinsic excitation given to the heavy fragment in panel (c) (88:148) can be understood from Fig. 4, and the fact that the light fragment receives the largest energy share in panel (f) (104:132) can be understood from Fig. 3, as discussed above.

C. Distortion energy

As discussed above, the distribution of intrinsic energy in a proto-fragment, E_i^{intr}, varies with the specified value of TKE. The fragment distortion energies, E_i^{dist}, are also sensitive to the specified TKE because the sum of the total collective kinetic energy and the total distortion energy must equal the total available energy minus the total intrinsic energy,

$$\mathrm{TKE} + E_L^{dist} + E_H^{dist} = Q_{LH}^* - E_{sc}^* . \qquad (5)$$

Consequently, at the highest values of TKE the energy balance does not leave much room for fragment distortion. Conversely, the lowest TKE values are associated with large elongations of the scission configurations and significant distortions of the proto-fragments. The relationship between TKE and the fragment distortion energies is illustrated in Fig. 5 for six different mass partitions, and the TKE dependence of the proto-fragment shapes is illustrated in Fig. 6 for the same cases.

The distortion energy resulting from a certain deformation change depends strongly on the structure of the specific fragment considered. For example, for the fragment ^{160}Sm a deformation change from the ground-state value $\varepsilon = 0.25$ to $\varepsilon = 0.0$ (Fig. 6a) yields a distortion energy of $E^{\mathrm{dist}} = 11$ MeV (Fig. 5a), while the same deformation change for ^{94}Kr (Fig. 6d) yields a much smaller distortion energy, $E^{\mathrm{dist}} = 3$ MeV (Fig. 5). This is because the deformation energy curve $U(\varepsilon)$ for ^{160}Sm has a robust (i.e. stiff) prolate minimum, while that for ^{94}Kr is rather soft around its prolate minimum (with respect to both ε and γ).

For all mass partitions, the distortion energy of the heavy fragment is consistently larger than that of the light fragment, $E_{\mathrm{H}}^{\mathrm{dist}} > E_{\mathrm{L}}^{\mathrm{dist}}$. This difference grows with increasing mass asymmetry and the largest difference is found for $A_{\mathrm{L}} : A_{\mathrm{H}} = 76 : 160$, while there is almost no difference for $A_{\mathrm{L}} : A_{\mathrm{H}} = 94 : 142, 100 : 136, 104 : 132$.

We also note that the distortion energy is systematically smaller than the intrinsic energy for given fragment mass partition and TKE, $E_i^{\mathrm{dist}} < E_i^{\mathrm{intr}}$, but the relative contribution from the distortion energy to the total excitation energy of a fragment varies substantially from one fragment to another. For example, for $A_{\mathrm{L}} : A_{\mathrm{H}} = 94 : 142$ both fragments receive only 10–15% from the distortion energy, while for 82 : 154 the light fragment receives almost half of its final excitation energy from the distortion energy at the lowest TKE values, (but the contribution drops to only about 10% at the highest TKE values).

In general, our results reveal a quite complex, structure-dependent variation of both the intrinsic energy and the distortion energy with the fragment identity as well as with TKE.

IV. NEUTRON MULTIPLICITIES

After the primary fission fragments have been fully accelerated by their mutual Coulomb repulsion and their shapes have relaxed to their equilibration form, they typically deexcite by (possibly sequential) neutron evaporation followed by photon radiation. The mean number of neutrons emitted from a particular fragment species, $\bar{\nu}_i$, presents a convenient (and observable) measure of the degree of its initial excitation, $E_i^* = E_i^{\mathrm{intr}} + E_i^{\mathrm{dist}}$.

Therefore, in the present study, we calculate neutron evaporation from the excited fragments. We employ the method described in Ref. [20], but use the effective micro-
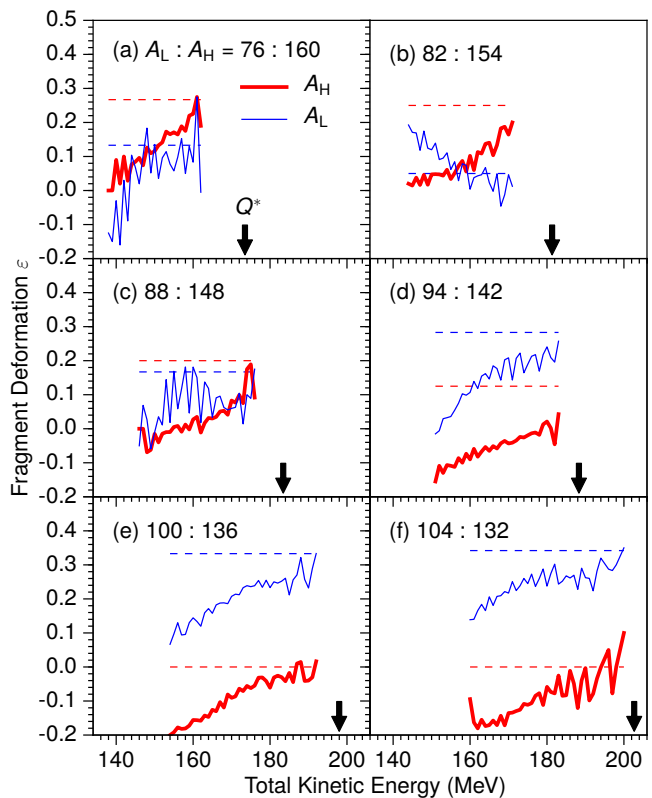

FIG. 6.   Average fragment deformations at scission versus the total kinetic energy for the same fragment combinations shown in Fig. 5. $E_{\mathrm{n}} = 0$. Thick red curves show the heavy fragment deformation and thin blue curves the light fragment deformation. Horizontal dashed red and blue lines show equilibrium deformations for the heavy and light fragments, respectively. The arrows point to the Q^* values. The jaggedness of the curves is caused by the finite sampling on a grid of 3QS shapes.

scopic level densities of the daughter nuclei (rather than the simplified Fermi-gas form), as in our earlier study [7]. Thus we assume that the kinetic energy spectrum of an evaporated neutron is given by

$$dN_{\mathrm{n}}(\epsilon_{\mathrm{n}})/d\epsilon_{\mathrm{n}} \sim \rho'(E'_{\mathrm{max}} - \epsilon_{\mathrm{n}})\,\epsilon_{\mathrm{n}}\ , \qquad (6)$$

where $E'_{\mathrm{max}} = E^* - S'_{\mathrm{n}}$ is the maximum excitation in the daughter nucleus (corresponding to the evaporation of a neutron having vanishing kinetic energy ϵ_{n}) and $\rho'(E')$ is its level density.

For thermal fission, $E_{\mathrm{n}} \approx 0$, the average neutron multiplicity from each fragment species is calculated for specified values of TKE (Sect. IV A) and for specified values of TXE (Sect. IV B). Corresponding results for $E_{\mathrm{n}} = 5.55$ MeV are presented subsequently (Sect. IV C).

A. TKE-gated neutron multiplicities

Figure 7 shows the calculated average neutron multiplicity for specified TKE from the light and the heavy

fragments, $\bar{\nu}(A_{\mathrm{L}};\mathrm{TKE})$ and $\bar{\nu}(A_{\mathrm{H}};\mathrm{TKE})$, as well as their sum, for the same six divisions as were considered in Figs. 5-6. Also shown (where available) are the experimental results reported by Göök et al. [8]. In general, the agreement between calculated and measured results is very good.

For very asymmetric divisions the heavy fragment receives most of the excitation energy (see Fig. 5) and, as a result, it contributes almost all of the neutrons. This feature is most pronounced for the most asymmetric case displayed, $A_{\mathrm{L}} : A_{\mathrm{H}} = 76 : 160$, but it is also clearly present for 82 : 154 and, to a smaller degree, for 88 : 148. For 94 : 142 the two mean multiplicities are very similar even though the heavy fragment is $\approx 50\%$ larger than the light one. Finally, closer to symmetry (100 : 136 and 104 : 132), where the microscopic effects tend to favor the light fragment in the energy division, the neutron multiplicity is dominated by the light fragment. This gradual change in the mean neutron multiplicity as a function of the mass asymmetry is also present in the TKE-averaged results, as was previously discussed [7].

The calculated dependence of the total excitation energy of a given fragment, $E_i^* = E_i^{\mathrm{intr}} + E_i^{\mathrm{dist}}$, on the specified value of TKE (Fig. 5), provides an understanding of how the mean neutron multiplicity varies with TKE for the various fragment masses. For the most asymmetric case considered, $A_{\mathrm{L}} : A_{\mathrm{H}} = 76 : 160$, 70-80% of the total excitation energy is carried by the heavy fragment. Because the light fragment is then typically insufficiently excited to permit the evaporation of a neutron, practically all of the neutrons originate from the heavy fragment, for all values of TKE (see Fig. 7a).

For several fragment combinations the $\bar{\nu}$ dependence of TKE is almost linear. An interesting exception is the threshold effect found for the light fragment in the 82 : 154 division (Fig. 7b), an effect also seen in the measurements [8]. For large values of TKE all neutrons are emitted from the heavy fragment, while the neutron emission from the light fragment sets in smoothly at lower TKE, resulting in a gradual increase of $\bar{\nu}_{\mathrm{L}}$ from zero to about one as TKE decreases from about 160 to 145 MeV (Fig. 7b).

For the 88 : 148 mass division the light fragment is calculated to emit on the average somewhat more than one neutron at the smallest TKE values, while the heavy fragment dominates, emitting up to about three neutrons at small TKE.

For $A_{\mathrm{L}} : A_{\mathrm{H}} = 94 : 142$ one third of the total excitation energy is concentrated in the light fragment at high TKE, and its share increases smoothly with decreasing TKE towards an equal share for both fragments at the smallest TKE. This is seen in Fig. 7d: at high TKE the neutron evaporation is coming only from the heavy fragment, but as TKE is decreased the ratio changes smoothly leading towards equal contributions from the light and heavy fragments at small TKE. To some degree, this is also seen in the measured neutron multiplicities.

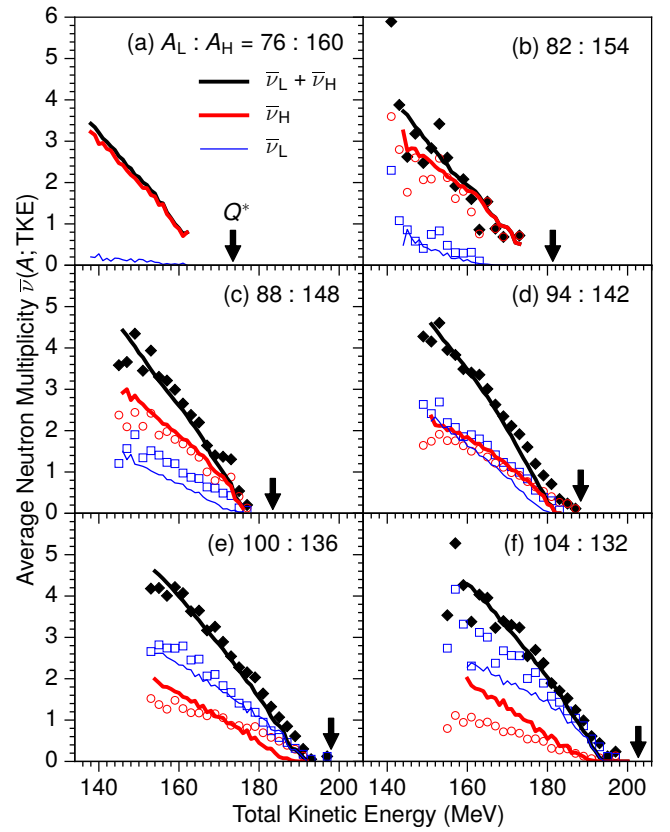For the two least asymmetric divisions, 100 : 136 and

FIG. 7. Calculated and measured average multiplicity of neutrons emitted from reaction ^{235}U(n_{th},f) versus TKE for the six fragment combinations of Fig. 5. Measured [8] light-fragment neutron multiplicity is shown by red circles, heavy-fragment neutron multiplicity by blue squares, and the total is shown by black squares. The calculated light-fragment neutron multiplicity is shown by thin blue lines, the heavy-fragment multiplicity is shown thick red lines, and the total multiplicity is shown by black lines. The arrows point to the Q^* values.

104 : 132, most neutrons are emitted from the light fragment. For these cases we have $\bar{\nu}_{\mathrm{L}} > \bar{\nu}_{\mathrm{H}}$ for all TKE values, with the difference decreasing with decreasing TKE for 104 : 132.

For this latter case, the calculations differ somewhat from the data, with the calculated $\bar{\nu}_{\mathrm{H}}$ exceeding the data for small TKE and the calculated $\bar{\nu}_{\mathrm{L}}$ being smaller than the data. It is interesting to note the non-linear variation of $\bar{\nu}_{\mathrm{L}}$ and $\bar{\nu}_{\mathrm{H}}$ with TKE, with $\bar{\nu}_{\mathrm{H}}$ approaching $\bar{\nu}_{\mathrm{L}}$ at small TKE. The partition of the intrinsic energy at scission, which dominates TXE for these fragments, provides the major part of the final excitation energy of the light fragment (see Figs. 3 and 5e). But the data suggests that the light fragment's share of the excitation energy is even larger. This may be because the dominant fission fragment having $A = 132$ is the doubly magic nucleus ^{132}Sn, while our requirement of a fixed N/Z ratio for all fragments yields ^{132}Te for $A = 132$. If the doubly magic nucleus ^{132}Sn is the principal heavy $A = 132$ fragment,

then its extraordinarily low level density would indeed cause the light fragment to receive an even larger share of the excitation energy.

B.   TXE-gated neutron multiplicities

When the total excitation energy TXE is fixed, then all different fragment pairs have the same amount of excitation energy to share (namely TXE), and it is instructive to study the neutron multiplicity $\bar{\nu}(A)$ from different fission fragments. In particular, this would make it possible to investigate the variation of $\bar{\nu}(A; \mathrm{TXE})$ as TXE is changed and study how the sawtooth feature evolves with excitation energy.

It is elementary to obtain $\bar{\nu}(A; \mathrm{TXE})$ from $\bar{\nu}(A; \mathrm{TKE})$ because $\mathrm{TXE} = Q^*_{\mathrm{LH}} - \mathrm{TKE}$ for a given light-heavy mass split, so $\bar{\nu}(A; \mathrm{TXE}) = \bar{\nu}(A; \mathrm{TKE} = Q^*_{\mathrm{LH}} - \mathrm{TXE})$ where the fragment mass number A determines the L-H division.

Figure 8 shows $\bar{\nu}(A; \mathrm{TXE})$ for four different values of the total excitation energy, TXE=15, 20, 25, 30 MeV. As discussed in detail above, the specified total excitation energy TXE is being divided quite unevenly between the two fragments due to the complexity of the separate contributions from intrinsic energy and distortion energy. For all four TXE values, the average neutron multiplicity from the light fragment, $\bar{\nu}_{\mathrm{L}}$, increases with the fragment mass number, A_{L}, while the multiplicity from the heavy partner fragment decreases (except for the cases $A_{\mathrm{L}} = 104$ and $A_{\mathrm{H}} = 160$). At large asymmetries the light fragment evaporates fewer neutrons than the heavy fragment, while the opposite is true closer to symmetry.

With increasing TXE the excitation energy of each fragment increases, resulting in larger neutron multiplicities from both fragments. However, the increase of the excitation energy of a fragment is not linear in TXE, as was discussed in Sects. III B and III C. For example, for $A_{\mathrm{L}} : A_{\mathrm{H}} = 104 : 132$ an increase of TXE by 5 MeV from 15 to 20 MeV results in an energy increase of about 3.5 MeV in the light fragment and 1.5 MeV in the heavy fragment, leading to multiplicity increases of about $\Delta\bar{\nu}_{\mathrm{L}}=0.6$ and $\Delta\bar{\nu}_{\mathrm{H}}=0.2$ (see Fig. 8). By contrast, the same increase in TXE from 25 to 30 MeV causes an energy increase of about 2.5 MeV in both fragments leading to $\Delta\bar{\nu}_{\mathrm{L}}=\Delta\bar{\nu}_{\mathrm{H}}=0.3$. This evolution away from light-fragment dominance with increasing TXE is caused primarily by the specific energy-dependence of the level densities in the distorted proto-fragments which reduces the favoring of the light fragment in the sharing of the intrinsic energy at scission, as is seen in Figs. 3b and 3c.

The neutron multiplicity from more asymmetric divisions show a less dramatic evolution with TXE. For example, for $A_{\mathrm{L}} : A_{\mathrm{H}} = 82 : 154$ the multiplicity increases are $\Delta\bar{\nu}_{\mathrm{L}}=0.1$ and $\Delta\bar{\nu}_{\mathrm{H}}=0.6$ when TXE is increased from 5 to 10 MeV, and $\Delta\bar{\nu}_{\mathrm{L}}=0.2$ and $\Delta\bar{\nu}_{\mathrm{H}}=0.4$ when TXE is increased from 25 to 30 MeV.

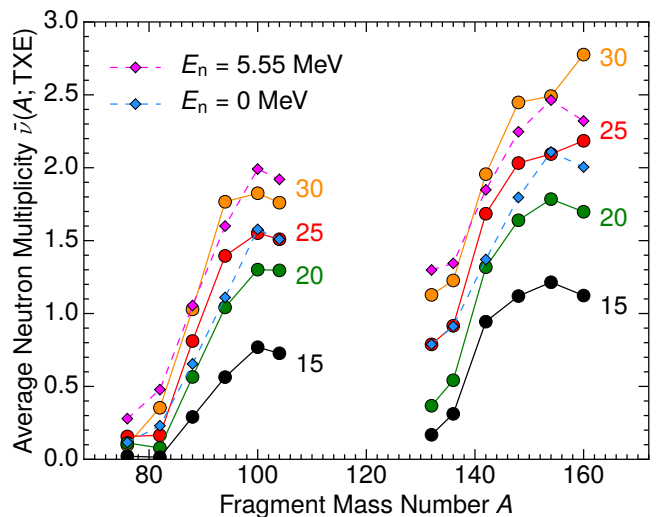When TXE is increased from 15 to 30 MeV for A_{L} :

FIG. 8.   Calculated average neutron multiplicity, $\bar{\nu}(A, \mathrm{TXE})$, for $^{235}\mathrm{U}(n_{\mathrm{th}}, f)$ for fixed values of TXE, is shown as function of the fission fragment mass number, A. Results are shown for four different TXE values, TXE=15, 20, 25 and 30 MeV (filled circles connected by solid lines). The neutron multiplicity averaged over TXE-values (eq. 7) is shown for E_{n}=0 (blue diamonds connected by dashed lines) and for E_{n}=5.55 MeV (purple diamonds connected by dashed lines).

$A_{\mathrm{H}} = 76 : 160$ almost all increase in excitation energy goes to the heavy fragment. This results in the large increase in heavy-fragment neutron multiplicity, $\Delta\bar{\nu}_{\mathrm{H}}$=1.7, as compared to only $\Delta\bar{\nu}_{\mathrm{L}}$=0.3 for the light fragment.

Figure 8 also shows the unconstrained neutron multiplicity, $\bar{\nu}(A)$, for both thermal fission, $E_{\mathrm{n}} \approx 0$, and for the higher energy considered in Sect. IV C, $E_{\mathrm{n}} = 5.55$ MeV. The unconstrained multiplicity can be regarded as a weighted average of the TXE-constrained multiplicity,

$$\bar{\nu}(A) = \frac{\int N(A; \mathrm{TXE})\, \bar{\nu}(A; \mathrm{TXE})\, d\mathrm{TXE}}{\int N(A; \mathrm{TXE})\, d\mathrm{TXE}} \ , \qquad (7)$$

where $N(A; \mathrm{TXE})$ denotes the number of events leading to the specified value of TXE. For thermal fission the average TXE value is found to be around 25 MeV for most the A values shown, except for $A_{\mathrm{L}} : A_{\mathrm{H}} = 88 : 148$ and $94 : 142$ where $\overline{\mathrm{TXE}} = 21 - 22$ MeV. We note that $\bar{\nu}(A)$ agrees very well with $\bar{\nu}(A; \overline{\mathrm{TXE}})$ for both thermal fission and for E_{n}=5.55 MeV for which we have $\overline{\mathrm{TXE}} \approx 30$ MeV.

C.   Higher neutron energies

We also discuss our results for a higher neutron energy, $E_{\mathrm{n}} = 5.55$ MeV. This neutron energy was previously considered in experiments [14], and is close to the maximal energy for first-chance fission.

Figure 9 shows the TKE-gated mean neutron multiplicity, $\bar{\nu}(A; \mathrm{TKE})$ for the same six mass divisions as
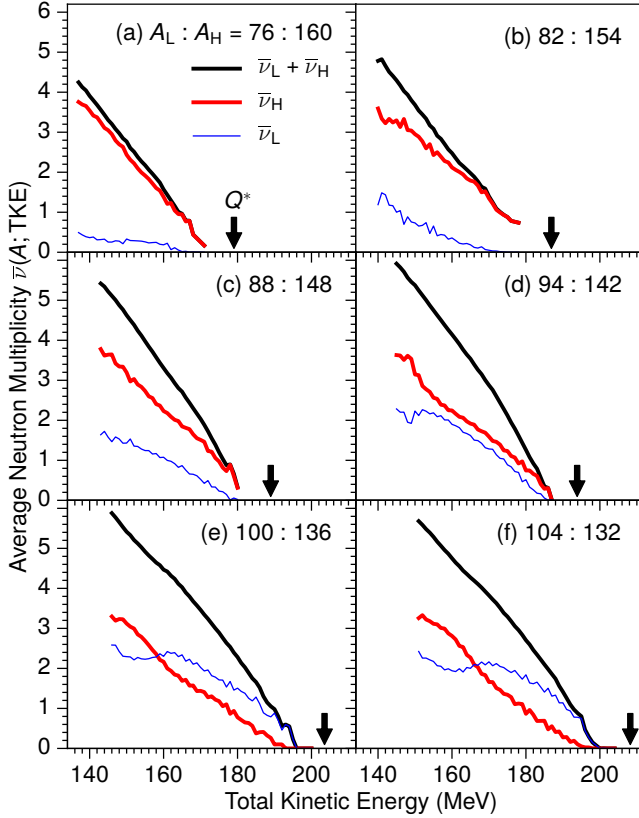
FIG. 9. Same as Fig. 7 but for E_n=5.55 MeV.

studied above. When the energy of the incoming neutron increases, the Q value increases correspondingly because the initial excitation energy of the fissioning nucleus is $E_0^* = S_\mathrm{n} + E_\mathrm{n}$. Thus TKE+TXE is increased by E_n and we find that the average TKE changes very little and most of the additional energy goes to TXE. As a consequence, the shape evolution is able to explore a wider domain of the potential-energy landscape and the system gains access to valleys that lead to more elongated scission shapes. This feature will be reflected in a bimodal character of the TKE distribution (see Sect. IV C 1).

For the three most asymmetric divisions, Figs. 9a-c, the behavior of $\bar\nu(A;\mathrm{TKE})$ is similar to the thermal result for both $\bar\nu_\mathrm{L}$ and $\bar\nu_\mathrm{H}$ (see Figs. 7a-c), except for an overall increase due to the increased excitation of the primary fission fragment. On average, the neutron multiplicity increases by 0.3-0.4 for both the light and the heavy fragments.

This smooth evolution with E_n may be contrasted with the behavior for the less asymmetric divisions (Figs. 9d-f) where qualitative changes are apparent. For the two least asymmetric cases, it is especially noticeable that $\bar\nu(A_\mathrm{L};\mathrm{TKE})$ and $\bar\nu(A_\mathrm{H};\mathrm{TKE})$ cross so the heavy fragment becomes dominant at low TKE, with the crossings occuring at TKE values of 160 and 164 MeV for 100 : 136 and 104 : 132, respectively. Such an evolution would be expected from the fact that the increased intrinsic ex-

citation of the proto-fragments tends to wash out the structure effects that favored the light fragment. In the next Section we discuss how the appearence of a new superlong fission mode plays an important role for this behavior.

1. Bimodal fission

Figure 10 shows the separate contributions to the final fragment excitation energy from their intrinsic and distortion energies at scission, displayed versus the resulting TKE for $A_\mathrm{L} : A_\mathrm{H} = 104 : 132$. As mentioned above, the increase in the kinetic energy of the incoming neutron primarily causes the intrinsic energy to increase and that in turn gives the system access to a wider variety of shapes during its evolution. This results in the appearance of a new fission mode characterized by more elongated scission shapes and, consequently, lower TKE values, see Fig. 2b. On average, the scission shapes of these events have $q_2 \approx 16.5$ significantly larger than those reached with thermal neutrons (Fig. 2a).

The existence of such a *superlong* (SL) fission mode has long been known [21]. The mode favours symmetric fission, and it is believed that the observed increase of emitted neutrons near symmetry with incident neutron energy is caused by an increase in the yield of the superlong mode, see e.g. Refs. [22, 23].

For the large elongations characterizing the superlong mode it is preferable for the heavy fragment to develop a large quadrupole deformation and in average we have ε_H=0.32. For small TKE values the average quadrupole moment of the heavy fragment is even larger, for example $\varepsilon_\mathrm{H} \approx 0.5$ at TKE=150 MeV. Also the light fragment is deformed, but with a smaller deformation, $\varepsilon_\mathrm{L} \approx 0.15$.

The scission shapes of the SL mode are compared in Fig. 2b with those obtained at higher TKE values where the elongation is much smaller, $q_2 \approx 10 - 12$. In the normal mode, the shape of the heavy fragment is slightly oblate, $\varepsilon_\mathrm{H} \approx -0.08$ while the light fragment has $\varepsilon_\mathrm{L} \approx 0.15$. We refer here to this fission mode as *standard* (St).

Figure 10 also shows calculated distributions of the two fission modes versus TKE. Guided by the result shown in Fig. 2b, the SL mode is defined by the condition $q_2 > 14$ and correspondingly the St mode is defined by $q_2 < 14$. The St mode exhibits a broad distribution with its maximum at TKE $\approx$ 180 MeV and completely dominates the fission process at high TKE. But with decreasing TKE values the SL mode gradually appears, at first partly overlapping with the St mode but then taking completely over in the lowest TKE range.

The maximum of the SL distribution occurs at TKE $\approx$ 164 MeV. This average TKE value for the SL mode, converted from fragment to product kinetic energy becomes 161 MeV, and is in reasonable agreement with the measured product kinetic energy for mass split $A_\mathrm{L} : A_\mathrm{H} = 104 : 132$, namely 156 MeV [24]. Also the calculated average TKE value for the St mode, 178 MeV, converted

to the product kinetic energy 176 MeV, is in good agreement with the corresponding measured value 174 MeV. Often [21, 24], the St mode is described as consisting of two modes, S1 and S2, which together account for the asymmetric fission, and the value 174 MeV is a weighted average over these modes from the results given in Ref. [24].

The SL mode has maximal influence for symmetric fission but is increasingly involved in more asymmetric fission splits with increasing neutron energy. For thermal neutrons the SL mode gives zero contribution to fission events with mass split $A_L : A_H = 104 : 132$, while the SL mode contributes about 10% of the events at $E_n = 5.55$ MeV, see Fig. 10. This agrees fairly well with data where the SL mode is found to contribute with 0% and 5% at $E_n \approx 2$ MeV and $E_n \approx 5$ MeV, respectively [24].

The large deformations of the heavy fragment in the SL mode implies very large distortion energies, E_H^{dist}=15-20 MeV for TKE=150-160 MeV, because the fragment shape has to relax from $\varepsilon_H = 0.4 - 0.5$ to its spherical ground-state shape. For comparison, the distortion energy of the heavy fragment in the St mode is only 2-3 MeV.

It is interesting to study how the partition of the intrinsic energy between the light and heavy fragments depends on the fission mode for mass division around A_L:A_H=104:132. In the St mode the heavy fragment has a small oblate deformation, close to its doubly magic spherical ground state. The spherical shell gaps at $Z = 50$ and $N = 82$ lead to a very low level density for the heavy fragment, causing the light fragment to be favored, see Fig. 3. On the other hand, in the SL mode the heavy fragment has a substantial quadrupole deformation. The proto-fragment is thus far away from equilibrium and has a large single-particle level density near the Fermi level, leading to a large total level density. The distribution function for the intrinsic energy at scission, Eq. (4), then somewhat favors the heavy fragment.

Relative to the St mode, the heavy fragment receives significantly more excitation energy in the SL mode due to two different mechanisms: First, as just discussed, it is the favored recipient of intrinsic energy at scission. Second, as also mentioned above, it is very distorted at scission and its shape relaxation leads to an additional significant contribution.

The increase of the neutron multiplicity from the heavy fragment with increasing incident energy is thus partly due to the appearance of the SL mode. For thermal fission only the St mode appears and $\bar{\nu}_L$ is larger than $\bar{\nu}_H$ for all TKE. With increasing neutron energy the SL mode appears and causes the heavy fragment to become preferentially more excited. Consequently, with increasing E_n, $\bar{\nu}_H$ increases faster than $\bar{\nu}_L$.

Although the above detailed analysis was carried out for the specific division A_L:A_H=104:132, it is expected to hold also for the neighbouring mass divisions, as is suggested by Fig. 9e for A_L:A_H=100:136. For this mass split we find about 5% SL mode at E_n=5.55 MeV that
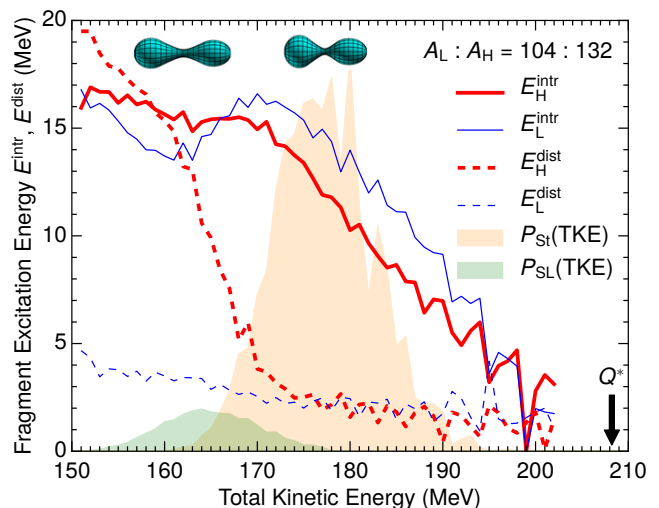

FIG. 10. Similar to Fig. 5f, with fragment mass ratio A_L:A_H=104:132, for E_n=5.55 MeV. Probability densities are shown for the two modes: superlong (SL), with average shape specified by q_2=16.5, ε_L=0.15, ε_H=0.32 (green area), and standard (St) with average shape q_2=11.5, ε_L=0.25, ε_H=-0.08 (orange area). Typical shapes of the SL and St modes are shown.

can be compared to data that gives 3% [24]. With the smaller contribution of the SL mode the dominance of $\bar{\nu}_H$ over $\bar{\nu}_L$ sets in at a lower TKE value for the mass split A_L:A_H=100:136 than for A_L:A_H=104:132 (Fig. 9e,f).

Indeed, it has been found experimentally [14] that the additional prompt neutrons emitted when the incident neutron energy is increased originate mainly from the heavy fragment. The onset of the SL mode with increasing neutron energy provides an additional mechanism for the neutron multiplicity from the heavy fragment to increase more than from the light fragment.

V. SUMMARY AND DISCUSSION

Based on macroscopic-microscopic potential-energy surfaces in the 3QS shape parametrization, and microscopic level densities, we have applied the Metropolis random walk method to treat the induced fission reaction ^{235}U(n,f) at E_n=0 and 5.55 MeV. Because the calculational method generates an ensemble of individual fission events it is possible to extract a large variety of correlations. We have particularly studied $\bar{\nu}(A; \text{TKE})$, the average neutron multiplicity as function of the primary fission-fragment mass number A for events leading to a specified total fragment kinetic energy TKE. For a given mass division, $A_0 \to A_L + A_H$, the TKE constraint restricts the total combined fragment excitation energy to be TXE = Q_{LH}^* − TKE. The excitation of each fragment is composed of two terms: its share of the total available intrinsic excitation energy at scission and the energy recovered from the relaxation of its distorted

shape of the proto-fragment. The division of the intrinsic excitation energy between the proto-fragments is carried out statistically based on their microscopic level densities. As a consequence, contributions to each fragment from the intrinsic excitation energy and the distortion energy vary with A and TKE in a non-trivial manner.

The indirect observation of the excitation energy in each primary fragment is made through the neutron multiplicity. For thermal fission, where TKE-gated data is available, a good agreement is obtained between the calculated and the measured $\bar{\nu}(A; \text{TKE})$. This agreement extends to a number of finer details, such as the threshold effect in neutron multiplicity from the light fragment with decreasing TKE in fission leading to the division $A_{\text{L}} : A_{\text{H}} = 82 : 154$. Certain differences between calculated and measured neutron multiplicity versus TKE for $A_{\text{L}} : A_{\text{H}} = 104 : 132$ may be due to the fact that the calculation assumes that all the fragments have the same N/Z ratio. The inclusion of the fragment isospin degree of freedom would probably make ^{132}Sn the most favored fragment, rather than the neighboring ^{132}Te, and, consequently, increase the difference between $\bar{\nu}(A_{\text{L}}; \text{TKE})$ and $\bar{\nu}(A_{\text{H}}; \text{TKE})$, as is experimentally observed.

We also studied $\bar{\nu}(A; \text{TXE})$, the mass-dependent average neutron multiplicity for events having the specified value of TXE, the combined excitation energy of the two primary fragments. This allows more detailed studies of the sawtooth behavior of $\bar{\nu}(A)$ with excitation energy.

An increase of the incident neutron energy to $E_{\text{n}} = 5.55$ MeV leads to the appearance of a new superlong fission mode characterized by low TKE values and occurring in the near-symmetric region, in agreement with experimental findings. In the SL fission events, which involve very elongated scission configurations, the heavy proto-fragment is particularly distorted, implying a large distortion energy, but also a high level density. For these reasons, most of the additional energy brought in by the neutron goes to excitation of the heavy primary fragment. Consequently, $\bar{\nu}_{\text{H}}$ increases faster than $\bar{\nu}_{\text{L}}$ with increasing E_{n}, as is also observed experimentally.

The appearance of the SL mode at higher neutron energies for the fission mass divisions $A_{\text{L}} : A_{\text{H}} = 104 : 132$ and $100 : 136$ is seen in the calculated correlated neutron multiplicity: With decreasing TKE, $\bar{\nu}(A_{\text{L}}; \text{TKE})$ and $\bar{\nu}(A_{\text{H}}; \text{TKE})$ cross so the heavy fragment grows dominant at low TKE (Fig. 10e,f). This prediction could be tested experimentally with correlation data obtained for higher neutron energies.

The region of symmetric fission was excluded in our present study because it appears that the scission configurations encountered for near-symmetric divisions are associated to too large TKE values. This may be because the employed 3QS shape parametrization is not sufficiently flexible to accommodate the rather elongated scission configurations. We are currently investigating this problem and hope to develop a suitable refinement.

Other models of the fission process, such as those employed in Refs. [3–6], suggest larger distortions of the proto-fragments than what was found in the present treatment. Those models may nevertheless be able to also give a reasonable reproduction of the measured neutron multiplicities if they compensate for the large distortion energies by giving correspondingly smaller intrinsic energies. In order to elucidate the situation, it would be very valuable to calculate within those models as well the TKE-constrained neutron multiplicities, $\bar{\nu}(A; \text{TKE})$. Detailed comparisons of this observable, both between the various models and with the experimental data, might reveal the quantitative importance of the different contributions to the fragment excitations and thus help to improve our understanding of the fission process.

[1] K. Nishio Y. Nakagome, H. Yamamoto, and I. Kimura, Nucl. Phys. A **632**, 540 (1998).

[2] B.D. Wilkins, E.P. Steinberg, and R.R. Chasman, Phys. Rev. C **14**, 1832 (1976).

[3] N. Dubray, H. Goutte, and J.-P. Delaroche, Phys. Rev. C **77**, 014310 (2008).

[4] G. Scamps and C. Simenel, Nature **564**, 382 (2018).

[5] A. Bulgac, P. Magierski, K.J. Roche, and I. Stetcu, Phys. Rev. Lett. **116**, 122504 (2016); A. Bulgac, S. Jin, and I. Stetcu, Phys. Rev. C **100**, 014615 (2019).

[6] A. Bulgac, S. Jin, K.J. Roche, N. Schunck, and I. Stetcu, Phys. Rev. C **100**, 034615 (2019).

[7] M. Albertsson, B.G. Carlsson, T. Døssing, P. Möller, J. Randrup, and S. Åberg, Phys. Lett. B **903**, 135276 (2020).

[8] A. Göök, F.-J. Hambsch, S. Oberstedt, and M. Vidali, Phys. Rev. C **98**, 044615 (2018); Alf Göök private communications (2020).

[9] J. Randrup and P. Möller, Phys. Rev. Lett. **106**, 132503 (2011).

[10] J. Randrup, P. Möller, and A.J. Sierk, Phys. Rev. C **84**, 034613 (2011).

[11] J. Randrup and P. Möller, Phys. Rev. C **88**, 064606 (2013).

[12] H. Uhrenholt, S. Åberg, A. Dobrowolski, T. Døssing, T. Ichikawa, and P. Möller, Nucl. Phys. A**913**, 127 (2013).

[13] D.E. Ward, B.G. Carlsson, T. Døssing, P. Möller, J. Randrup, and S. Åberg, Phys. Rev. C **95**, 024618 (2017).

[14] R. Müller, A.A. Naqvi, F. Käppeler, and F. Dickmann, Phys. Rev. C 29, 885 (1984).

[15] P. Möller, A.J. Sierk, T. Ichikawa, A. Iwamoto, R. Bengtsson, H. Uhrenholt, and S. Åberg, Phys. Rev. C **79**, 064304 (2009).

[16] J.R. Nix, Nucl. Phys. A **130**, 241 (1969).

[17] A. Tudora Eur. Phys. J. A 55, 98 (2019).

[18] A. Al-Adili, Ph.D Thesis, Uppsala University, p. 51

(2013); A. Oberstedt, private communications (2019).

[19] M.D. Usang, F.A. Ivanyuk, C. Ishizuka, and S. Chiba, Scientific Reports, 9:1525 (2019).

[20] J. Randrup, R. Vogt, Phys. Rev. C **80**, 024601 (2009).

[21] U. Brosa, S. Grossmann, and A.M. Müller, Physics Reports 197, 167 (1990).

[22] F.-J. Hambsch, S. Oberstedt, A. Tudora, G. Vladuca, and I. Ruskov, Nucl. Phys. A **726**, 248 (2003).

[23] K.H. Schmidt and B. Jurado, Phys. Rev. Lett. 104, 212501 (2010).

[24] R. Yanez, W. Loveland, J. King, J.S. Barrett, N. Fotiades, and H.Y. Lee, arXiv.1605.09690v4 (2017).